ARTICLE

Chinese Journal of Structural Chemistry

Monodispersed SWNTs Assembled Coating Layer as an Alternative to Graphene with Enhanced Alkali-ion Storage Performance

Chaoying Wang[1,3], Qianqian Yao[2], Yanmei Gan[2], Qixin Zhang[1], Lunhui Guan[3] and Yi Zhao[1,2*]

[1]*College of Chemistry and Materials Science, Fujian Normal University, Fuzhou 350007, China*

[2]*Straits Institute of Flexible Electronics (SIFE, Future Technologies), Fujian Normal University, Fuzhou 350117, China*

[3]*CAS Key Laboratory of Design and Assembly of Functional Nanostructures, Fujian Key Laboratory of Nanomaterials, Fujian Institute of Research on the Structure of Matter, Chinese Academy of Sciences, Fuzhou 350108, China*

ABSTRACT Graphene coating is commonly used to improve the performance of electrode materials, while its steric hindrance effect hampers fast ion transport with compromised rate capability. Herein, a unique single-walled carbon nanotubes (SWNTs) coating layer, as an alternative to graphene, has been developed to improve the battery behavior of iron-based anodes. Benefiting from the structure merits of mesoporous SWNTs layer for fast electron/ion transport and hollow Fe_3O_4 for volume accommodation, as-prepared Fe_3O_4@SWNTs exhibited excellent lithium storage performance. It delivers a high capacity, excellent rate capability, and long lifespan with capacities of 582 mA·h·g^{-1} at 5 A·g^{-1} and 408 mA·h·g^{-1} at 8 A·g^{-1} remained after 1000 cycles. Such performance is better than graphene-coated Fe_3O_4 and other SWNT-Fe_3O_4 architectures. Besides, SWNTs coating is also used to improve the sodium and potassium storage performance of $FeSe_2$. The kinetics analysis and ex-situ experiment further reveal the effect of SWNTs coating for fast electron/ion transfer kinetics and good structure stability, thus leading to the superior performance of SWNTs-coated composites.

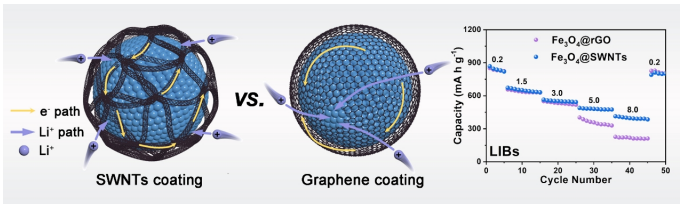

Keywords: single-walled carbon nanotubes, graphene, Fe_3O_4, $FeSe_2$, alkali-ion batteries

n INTRODUNTION

Lithium-ion batteries (LIBs) are widely used in portable electronics, electric vehicles, and smart grids for decades.[1] Recently, sodium-ion batteries (SIBs) and potassium-ion batteries (PIBs) have attracted a great deal of attention owing to their advantage of abundant resources and low cost, and are considered as alternative systems to LIBs for large-scale energy storage.[2-4] To fulfill the increasing demand of energy storage, next-generation alkali-ion batteries require high performance in energy/power density, cycling life, and safety. The development of superior electrode materials makes an important role to achieve this goal. In terms of anode materials, conversion-type metal oxides/sulfides/selenides are in hot discussion due to their high theoretical capacity, environ benign, and low cost.[5-8] For instance, Fe_3O_4 is one of the most explored anode materials due to its high theoretical capacity of 926 mA·h·g^{-1}. Nevertheless, their instinct poor conductivity and large volume changes during cycles would result in the fast capacity decay and poor rate behavior, thus hampering the practical application of these materials.

To solve these issues, the combination of high-capacity anodes and carbon matrix with rational microstructure design has been demonstrated to be an effective tactic.[9-14] Especially, carbon-coated hollow structure can display excellent electrochemical performance.[15,16] This structure can provide interior void room to tolerate the volume variation, and outer protection layer to enhance the electronic conductivity and prevent the aggregation of active material. So far, the most reported carbon layers are amorphous-carbon and graphene.[17-24] For instance, Zhu et al. reported a carbon coated Fe_2O_3 hollow structure for lithium storage, which can deliver more excellent cycling retention and rate behavior than pure Fe_2O_3.[25] The graphene-coated Fe_3O_4 composite sustained a capacity of 708 mA·h·g^{-1} at 0.4 A·g^{-1} after 300 cycles and a rate capacity of ~490 mA·h·g^{-1} at 1 A·g^{-1}.[26] However, the amorphous carbon usually shows poor electrical conductivity, and the planar structure of graphene would block the fast ion transport with long diffusion path.[27,28] These drawbacks hamper the further enhancement of rate capability and cyclic life for hollow structured composites. Therefore, it is of great vital to fabricate superior coating layer with both good conductivity and fast ion transportation for excellent performance.

Herein, we reported a unique single-walled carbon nanotubes (SWNTs) coating layer, which was assembled by Hummer's method-derived monodispersed SWNTs, for enhancing the battery performance of conversion-type anode materials. Such SWNTs layer can effectively improve the electrical conductivity of active materials, and its mesoporous structure enabled the free transport of Li^+ from electrolyte to Fe_3O_4. Thus, as-prepared hollow Fe_3O_4@SWNTs exhibited high lithium storage capacity and long-term cycling performance with capacities of 582 mA·h·g^{-1} at 5 A·g^{-1} and 408 mA·h·g^{-1} at 8 A·g^{-1} sustained after 1000 cycles. The rate capacity of Fe_3O_4@SWNTs (397 mA·h·g^{-1} at 8 A·g^{-1}) was better than that of graphene coated Fe_3O_4 (216 mA·h·g^{-1}). Besides, $FeSe_2$@SWNTs also displayed much enhanced battery performance than $FeSe_2$ and graphene coated $FeSe_2$ for SIBs and PIBs. Moreover, ex-situ characterization and kinetics analysishave been carried out to explore the origin of good performancefrom SWNTs coating.

n RESULTS AND DISCUSSION

Figure 1a illustrates the fabrication process of SWNTs coating on hollow Fe_3O_4 particles. Firstly, commercial SWNTs bundle was chemically treated with a modified Hummer's method to prepare

DOI: 10.14102/j.cnki.0254-5861.2021-0050

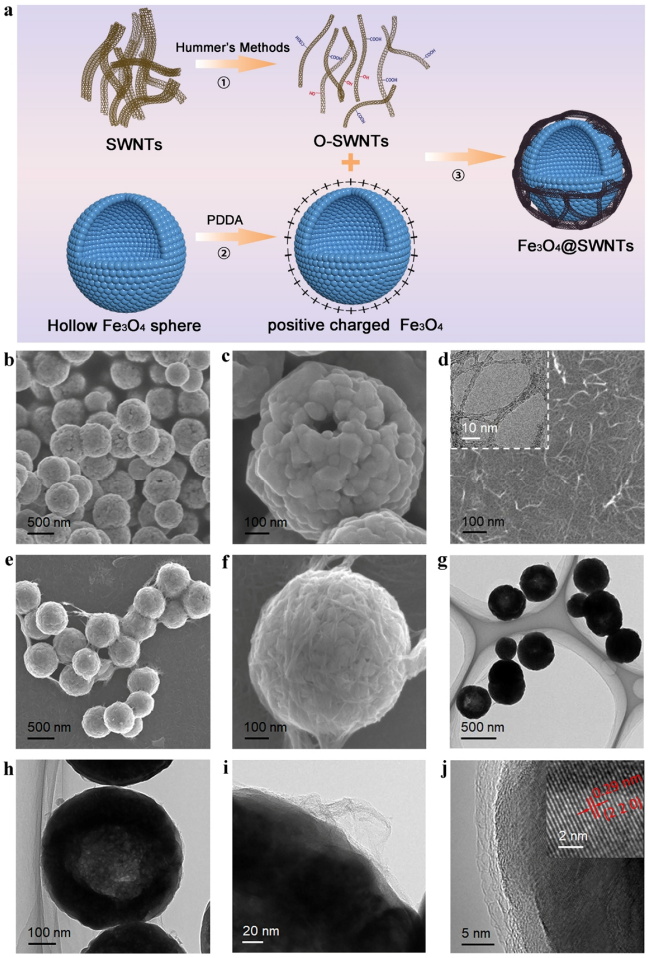

Figure 1. (a) Schematic illustration for the fabrication of Fe_3O_4@SWNTs composite. SEM images of (b–c) hollow Fe_3O_4, and (d) O-SWNT. (e–f) SEM, (g–j) TEM of Fe_3O_4@SWNT composite. Inset in (d) and (j) are the TEM image of O-SWNT and HRTEM image of Fe_3O_4.

monodispersed SWNTs with rich hydroxyl and carboxyl groups, denoted as O-SWNTs.[29] The hollow Fe_3O_4 was synthesized via a solvothermal method, followed with a PDDA modification.[18] The SWNTs coating on hollow Fe_3O_4 was achieved by the electrostatic adsorption between negatively charged O-SWNT and positively charged PDDA-Fe_3O_4, and then further annealed at 300 °C for 1 h in Ar.[30] Figure 1b–j display the SEM and TEM images of hollow Fe_3O_4, O-SWNT, and Fe_3O_4@SWNT composites. The SEM images in Figure 1b–c show the hollow structure of Fe_3O_4 particles with size around 600–800 nm. Figure 1d discloses the monodisperse one-dimensional structure of O-SWNTs, which is totally different with the SWNT bundles. The inset TEM image shows its average diameter of ~1.4 nm. Seen from Figure 1e–f, the surface of Fe_3O_4 particle was fully covered with a thin and mesoporous SWNTs coating layer. Obviously, TEM images of Fe_3O_4@SWNTs (Figure 1g–j) further reveal the hollow structure of Fe_3O_4 and the perfect coating of SWNTs layer. Inset of Figure 1j exhibits a regular interlayer spacing of 0.29 nm, assigned to the (220) plane of Fe_3O_4. As a comparison, hollow Fe_3O_4 particles were wrapped with GO followed by reduction at 300 °C to form Fe_3O_4@rGO composite (Figure S1).

X-ray diffraction (XRD) was carried out to clarify the crystalline

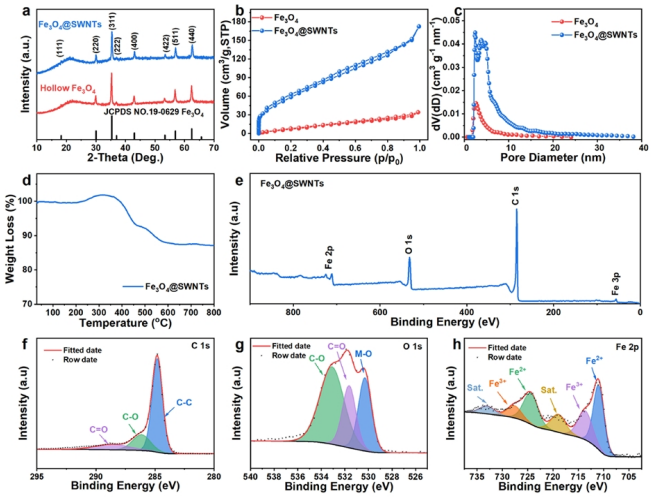

Figure 2. (a) XRD pattern, (b) nitrogen adsorption-desorption isotherms, (c) pore size distribution of Fe_3O_4 and Fe_3O_4@SWNTs. (d) TGA curve of Fe_3O_4@SWNT composite. (e) Survey XPS spectrum of Fe_3O_4@SWNTs and its high-resolution XPS spectra of (f) C 1*s*, (g) O 1*s*, and (h) Fe 2*p*.

structure of as-prepared composites. In Figure 2a, both of hollow Fe_3O_4 and Fe_3O_4@SWNT exhibited the typical diffraction peaks at 30.1°, 35.4°, 43.0°, 56.9° and 62.5°, which were well assigned to the (220), (311), (400), (511), and (440) planes of cubic spinel Fe_3O_4 (JCPDS No. 19-0629). Nitrogen adsorption-desorption isotherms were conducted to explore the surface area and pore structure of the samples in Figure 2b. As can be seen, Fe_3O_4@SWNTs exhibited a large surface area of 217.5 $m^2 \cdot g^{-1}$ and high pore volume of 0.226 $cm^3 \cdot g^{-1}$, larger than the values of Fe_3O_4 (36 $m^2 \cdot g^{-1}$ and 0.045 $cm^3 \cdot g^{-1}$) and Fe_3O_4@rGO (42 $m^2 \cdot g^{-1}$ and 0.044 $cm^3 \cdot g^{-1}$ in Figure S2). The pore size distribution was obtained from adsorption isotherm through Quenched solid density functional theory (QSDFT) model. Figure 2c discloses the mesopores of 2.4 and 3.8 nm in Fe_3O_4@SWNTs composite. Such high surface area and abundant pore structure of Fe_3O_4@SWNTs were derived from the mesoporous property of SWNTs coating and hollow structure of Fe_3O_4. As a result, it can provide efficient void space for volume variation and sufficient diffusion path for Li^+ diffusion, which was beneficial for the good structure stability and superior charge transportation during cycles.

The weight content of SWNTs was determined through TGA experiment. In Figure 2d, the weight increase before 315 °C and the subsequent weight loss were due to the oxidation of Fe_3O_4 to Fe_2O_3 and the oxidation of the SWNTs layer, respectively. Thus, the loading ratio of SWNTs was calculated to be 15.8 wt% in Fe_3O_4@SWNTs, which was similar with the 15.4 wt% content of rGO in Fe_3O_4@rGO composite (Figure S2b). Figure S3 shows the Raman spectrum of as-prepared composites. As can be seen, the I_D/I_G values of Fe_3O_4@SWNTs and Fe_3O_4@rGO were 0.62 and 0.93, respectively, implying the higher graphitization degree and better conductivity of SWNTs layer than rGO layer.[31] Figure 2e displays the survey XPS spectrum of Fe_3O_4@SWNTs composite, disclosing its component of C, O, and Fe elements. The spectrum of C 1*s* (Figure 2f) was divided into three peaks at 284.8, 286.1, and 288.7 eV, corresponding to C–C, C–O, and C=O bonds, respectively.[32] Three peaks located at 530.4, 531.6, and 533.1 eV can be observed in O 1*s* spectrum (Figure 2g), which were ascri-

DOI: 10.14102/j.cnki.0254-5861.2021-0050

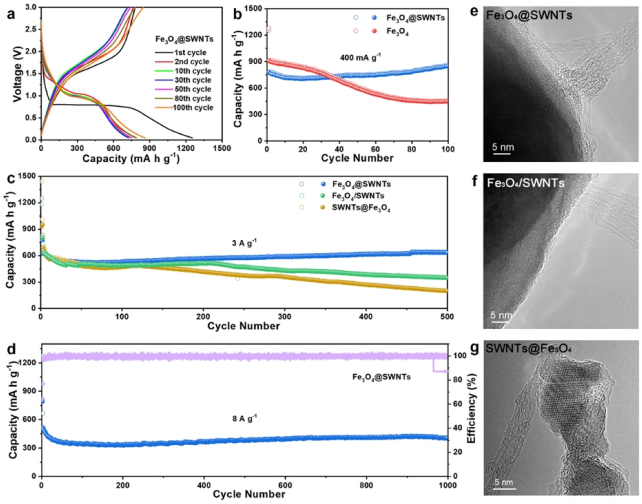

Figure 3. Lithium storage performance of Fe_3O_4-SWNT composites under various architectures. (a) Galvanostatic discharge/charge profiles of Fe_3O_4@SWNTs electrode for selected cycles at 400 mA·g^{-1}. (b) Cycling stability of Fe_3O_4 and Fe_3O_4@SWNTs at 400 mA·g^{-1}. (c) Cycling performance of Fe_3O_4@SWNTs, Fe_3O_4/SWNTs, and SWNTs@Fe_3O_4 composites with various microstructures at 3 A·g^{-1}. (d) Long-term cycling behavior of Fe_3O_4@SWNTs composite at a large current density of 5 A·g^{-1}. TEM images of (e) Fe_3O_4@SWNTs, (f) Fe_3O_4/SWNTs, (g) SWNTs@Fe_3O_4 composites.

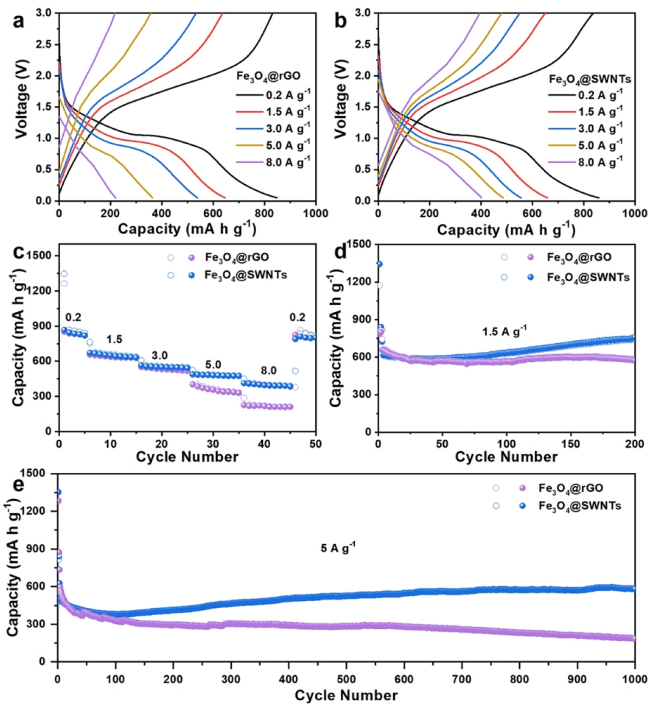

Figure 4. Lithium storage behavior comparison of Fe_3O_4@rGO and Fe_3O_4@SWNTs composites. Discharge/charge profiles under various rates of (a) Fe_3O_4@rGO and (b) Fe_3O_4@SWNTs electrodes. (c) Rate capability from 0.2 to 8.0 A·g^{-1}, (d) cycling performance at 1.5 A·g^{-1}, and (d) long-term cycling behavior at 5 A·g^{-1} of Fe_3O_4@rGO and Fe_3O_4@SWNTs electrodes.

bed to the Fe–O, C–O, and C=O, respectively.[33] Figure 2h exhibits the typical peaks of Fe^{2+} at 711.0 and 724.4 eV and Fe^{3+} at 714.3 and 727.4 eV, along with two shakeup satellite peaks at 720 and 733 eV.[30]

The lithium storage behavior of Fe_3O_4@SWNTs composite was investigated in Figure 3. For better comparison, two other SWNTs-based architectures were synthesized. As shown in Figure S4, Fe_3O_4/SWNTs composite was synthesized by simply mixing Fe_3O_4 particles with SWNTs.[34] For SWNTs@Fe_3O_4 sample, small Fe_3O_4 nanoparticles were anchored on the surface SWNTs.[35] The XRD pattern of SWNT@Fe_3O_4 in Figure S5 shows small and broad diffraction peaks, further illuminating the small size of Fe_3O_4. Figure S6a presents the cyclic voltammetry (CV) curves of Fe_3O_4@SWNTs electrode at 0.2 mV·s^{-1} from 0.05 to 3.0 V. During the first cathodic scan, the prominent peak at 0.52 V was attributed to the reduction of high valent Fe^{3+} and Fe^{2+} to Fe^0 and the irreversible formation of solid-electrolyte interphase (SEI) film on electrode.[36] In the following cathodic scans, the cathodic peaks moved to a higher voltage near 0.9 V, probably due to the improved kinetics. The anodic process of the CV curves almost overlapped, and the two broad peaks near 1.7 and 1.9 V could be assigned to the reversible oxidization of Fe^0 to Fe^{2+} and Fe^{3+}. The initial discharge and charge profiles of Fe_3O_4@SWNTs in Figure 3a delivered capacities of 1253 and 780 mA·h·g^{-1} at 400 mA·g^{-1}, respectively. The capacity loss in the first cycle can be assigned to the irreversible formation of SEI layer and incomplete decomposition of Li_2O.[37] Decreasing the amount of SWNTs or prelithiation strategy could be used to enhance the initial columbic efficiency. The following cycles can maintain similar shape and high capacities, implying the good cyclic stability of Fe_3O_4@SWNTs. Figure 3b illustrates the cycling behavior of Fe_3O_4 and Fe_3O_4@SWNTs electrodes at 400 mA·g^{-1}. Fe_3O_4@SWNTs manifested much better cycling stability and higher capacities than Fe_3O_4. It was capable of delivering a high capacity of 860 mA·h·g^{-1} after 100 cycles, higher than the value of 452 mA·h·g^{-1} for pure Fe_3O_4.

Figure 3c compares the cycling performance of Fe_3O_4@SWNTs, Fe_3O_4/SWNTs, and SWNTs@Fe_3O_4 composites at 3 A·g^{-1}, which were activated at a low current density of 0.2 A·g^{-1} in the initial two cycles. The HRTEM images in Figure 3e–g clearly illustrate the different microstructures between SWNTs and Fe_3O_4. Seen from Figure 3c, these electrodes exhibited similar good cycling retention in the initial cycles due to the presence of SWNT substrate. After that, Fe_3O_4/SWNTs and SWNTs@Fe_3O_4 electrodes underwent gradual capacity fading and kept low capacities of 347 and 201 mA·h·g^{-1} after 500 cycles, respectively. Such poor capacity retention in long-term cycles was attributed to large volume changes of Fe_3O_4 induced particle aggregation and pulverization. For Fe_3O_4@SWNTs, the hollow Fe_3O_4 and uniform SWNTs can effectively tolerate the volume fluctuation of Fe_3O_4 and prevent it from aggregation, thus benefiting for the excellent structure stability during cycles. Therefore, it can display outstanding cycling behavior, which maintained high capacities of 634 mA·h·g^{-1} after 500 cycles at 3 A·g^{-1} and 408 mA·h·g^{-1} after 1000 cycles at 8 A·g^{-1}. The different cycling stability of these three composites can be also observed in the discharge/charge profiles of various cycles (Figure S6). Compared with the as-reported Fe_3O_4/SWNTs mixtures, our Fe_3O_4@SWNTs composite with a fully covered SWNTs layer enabled a significant enhanced cycling life from 100–200 cycles

DOI: 10.14102/j.cnki.0254-5861.2021-0050

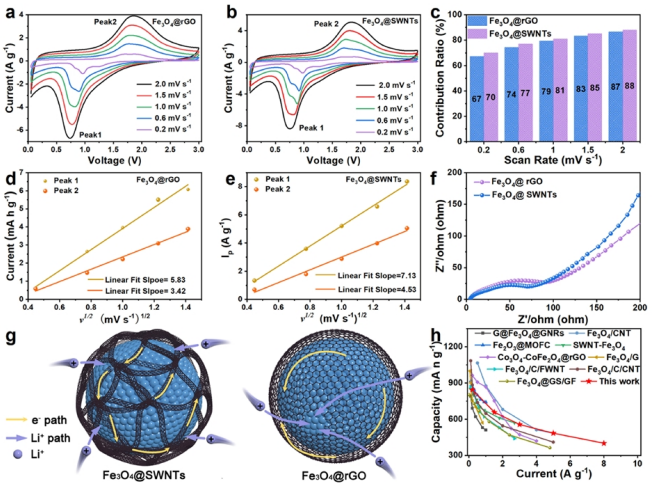

Figure 5. Kinetic analysis of Fe_3O_4@rGO and Fe_3O_4@SWNTs electrodes. CV curves at different scan rates from 0.2 to 2.0 mV·s^{-1} of (a) Fe_3O_4@rGO, (b) Fe_3O_4@SWNTs, and (c) their contribution ratio of pseudo capacitance under various scan rates. Peak current *vs.* $i^{1/2}$ and the corresponding linear fits of (d) Fe_3O_4@rGO and (e) Fe_3O_4@SWNTs electrodes. (f) EIS profiles after 15 cycles of these two electrodes. (g) Schematic diagram of the electron/ion transportation path for Fe_3O_4@rGO and Fe_3O_4@SWNTs. (h) Comparison of rate capabilities between Fe_3O_4@SWNTs and the as-reported anode materials for LIBs.

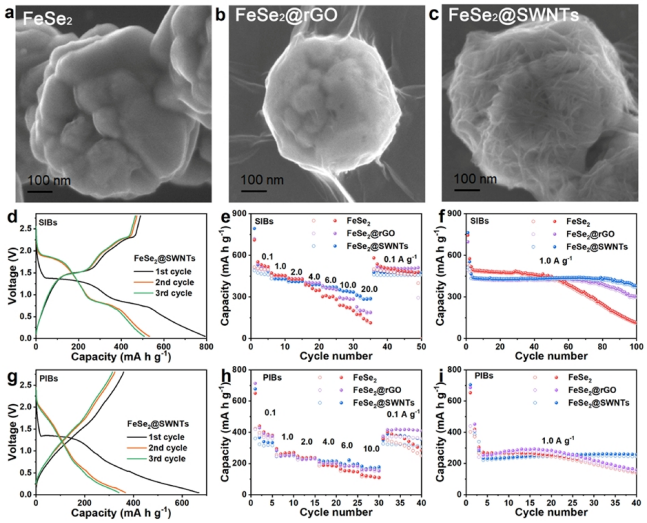

Figure 6. SEM images of (a) $FeSe_2$, (b) $FeSe_2$@rGO, (c) $FeSe_2$@SWNTs composites. (d, g) Discharge and charge curves in the initial three cycles of $FeSe_2$@SWNTs at 0.1 A·g^{-1}, (e, h) rate capability from 0.1 to 20 A·g^{-1}, and (f, i) cycling performance at 1 A·g^{-1} of $FeSe_2$@SWNTs, $FeSe_2$@rGO, and $FeSe_2$ electrodes for (d–f) SIBs and (g–i) PIBs.

to 1000 cycles.[34,38,39]

The lithium storage behavior of Fe_3O_4@rGO and Fe_3O_4@SWNTs was compared in Figure 4. Figure 4a–b shows the typical discharge/charge profiles of these two electrodes under various rates. These samples exhibited similar profile shape in the low current densities. However, Fe_3O_4@SWNTs exhibited lower overpotentials and higher capacities than Fe_3O_4@rGO at high rates. In Figure 4c, Fe_3O_4@SWNTs can maintain high average capacities of 840, 649, 551, 480, and 397 mA·h·g^{-1} at 0.2, 1.5, 3, 5 and 8 A·g^{-1}, respectively. When back to 0.2 A·g^{-1}, the capacity recovered to a high value of 815 mA·h·g^{-1}. However, Fe_3O_4@rGO only delivered poor rate capacities of 357 and 216 mA·h·g^{-1} at large current densities of 5 and 8 A·g^{-1}. Besides, SWNTs coating can result in better cycling behavior than rGO coated samples at high rates. Seen from Figure 4d–e and Figure S7, Fe_3O_4@SWNT can sustain high capacities of 759 mA·h·g^{-1} after 200 cycles at 1.5 A·g^{-1} and 582 mA·h·g^{-1} after 1000 cycles at 5 A·g^{-1}, outperforming the values of 572 and 185 mA·h·g^{-1} for Fe_3O_4@rGO.

In order to explore the origin of excellent performance for Fe_3O_4@SWNTs composite, CV profiles from 0.2 to 2.0 mV·s^{-1} were applied to investigate its kinetic process. Figure 5a–b exhibits the CV profiles of Fe_3O_4@rGO and Fe_3O_4@SWNTs, which display similar shapes under various rates. In general, the current (i) and scan rate (v) of CV curve obey the following equation:[40]

$$i(V) = k_1 v^{1/2} + k_2 v \quad (1)$$

Here k_1 and k_2 are the constants at a fixed potential, v is the sweep rate, and $k_1 v^{1/2}$ is the diffusion-controlled part and $k_2 v$ is the pseudocapacitance one. As shown in Figure 5c, the pseudocapacity contribution ratios of Fe_3O_4@SWNTs gradually increased with increasing the sweep rate and were higher than the values for Fe_3O_4@rGO electrode. The pseudocapacity ratio of Fe_3O_4@SWNTs reached up to 88% at 2.0 mV·s^{-1} (Figure S8), manifesting that its lithium storage process at high rates was dominated by the capacitance reaction. In addition, we also compared Li^+ diffusion coefficient (D_{Li^+}) of Fe_3O_4@rGO and Fe_3O_4@SWNTs through the simplified equation:[41-43]

$$i_p = a\sqrt{D}\sqrt{v} \quad (2)$$

In this equation, i_p and v are the peak current and scan rate, and a is a constant under the same test conditions. Based on the linear fit slopes in Figure 5d–e, the D_{Li^+} of Fe_3O_4@SWNTs was 1.5–1.8 times larger than that of Fe_3O_4@rGO. Furthermore, electrochemical impedance spectroscopy (EIS) of these two electrodes (Figure 5f) was also performed after 15 cycles. Fe_3O_4@SWNTs showed a smaller semicircle diameter than Fe_3O_4@rGO in the high-medium frequency region, indicating the low charge transfer impedance of SWNTs coating during cycles. The above results illuminated that the mesoporous SWNTs layer can not only enhance the electrical conductivity, but also enable the free transport of Li^+ from electrolyte to Fe_3O_4 (Figure 5g), thus accounting for the superior rate capability of Fe_3O_4@SWNTs composite. However, the steric hindrance effect of graphene retards fast Li^+ ion transport, resulting in the long diffusion path and large charge transfer resistance of Fe_3O_4@rGO composite with limited rate behavior.[27] As compared in Figure 5h and Table S1, our Fe_3O_4@SWNTs exhibited one of the best rate capacities and cycling retention among the as-reported Fe_3O_4-based and graphene-coated anodes for LIBs.

To further verify the structural stability of SWNTs coated sample, we investigated the morphology evolution of Fe_3O_4 and Fe_3O_4@SWNTs electrodes after 50 cycles. Seen from Figure S9, Fe_3O_4@SWNTs composite can retain original sphere morphology, while obvious cracking and particle agglomeration were observed in hollow Fe_3O_4 electrode. Based on the above characterizations, the superior lithium storage behavior of Fe_3O_4@SWNTs can be attributed to the following reasons: 1) the hollow structure of Fe_3O_4 can provide enough void space to tolerate its volume variation; 2) the outer SWNT coating can effectively hamper the aggre-

DOI: 10.14102/j.cnki.0254-5861.2021-0050

gation of Fe_3O_4 during repeated cycles, thus leading to good structure stability and long-term cycling life; 3) the large surface area of this composite can increase the contact area between electrolyte and electrode and facilitate the surface capacitance effect; 4) the mesoporous SWNT coating can improve the electrical conductivity and facilitate the fast Li-ion transportation, which boosts the charge transfer kinetics with superior rate capability.

Moreover, SWNTs coating was also applied to enhance the sodium and potassium storage behavior of $FeSe_2$ due to its better reaction kinetics with Na^+ and K^+ than Fe_3O_4.[44,45] Figure 6a shows the microsphere morphology of $FeSe_2$ with diameter around 500–800 nm. Then, the surface of $FeSe_2$ sphere was coated with rGO and SWNTs layer to form $FeSe_2$@rGO (Figure 6b and S10) and $FeSe_2$@SWNTs (Figure 6c and S11) composite, respectively. All the three samples exhibited typical XRD peaks $FeSe_2$ (JCPDS No. 79–1892) in Figure S12. For sodium storage (Figure d–f), $FeSe_2$@SWNTs exhibited an initial charge capacity of 490 $mA{\cdot}h{\cdot}g^{-1}$ at 0.1 $A{\cdot}g^{-1}$, and excellent rate capacities of 437, 413, 391, 371 and 342 $mA{\cdot}h{\cdot}g^{-1}$ at 1, 2, 4, 6, and 10 $A{\cdot}g^{-1}$, respectively. Even at 20 $A{\cdot}g^{-1}$, it still sustained a high reversible capacity of 295 $mA{\cdot}h{\cdot}g^{-1}$, higher than that of $FeSe_2$@rGO (202 $mA{\cdot}h{\cdot}g^{-1}$), $FeSe_2$ (148 $mA{\cdot}h{\cdot}g^{-1}$), and as-reported $FeSe_2$-based composites.[41,46] When cycled at 1 $A{\cdot}g^{-1}$, $FeSe_2$@SWNT can maintain a high capacity of 381 $mA{\cdot}h{\cdot}g^{-1}$ after 100 cycles, outperforming $FeSe_2$@rGO (308 $mA{\cdot}h{\cdot}g^{-1}$) and $FeSe_2$ (116 $mA{\cdot}h{\cdot}g^{-1}$) electrodes (Figure 6f and Figure S13). For potassium storage in Figure 6g–i, the $FeSe_2$@SWNTs also exhibited the best rate behavior and cycling stability among these composites. As shown in Figure 6h, $FeSe_2$@SWNTs, $FeSe_2$@rGO and $FeSe_2$ displayed the rate capacities of 171, 159, and 118 $mA{\cdot}h{\cdot}g^{-1}$ at 10 $A{\cdot}g^{-1}$, respectively. $FeSe_2$@SWNTs showed good cyclic retention and maintained a reversible capacity of 259 $mA{\cdot}h{\cdot}g^{-1}$ after 40 cycles at 1 $A{\cdot}g^{-1}$ in Figure 6i and Figure S14, while $FeSe_2$@rGO and $FeSe_2$ underwent poor cycling behavior and kept low capacities of 160 and 152 $mA{\cdot}h{\cdot}g^{-1}$ after 40 cycles. The limited cyclic life of $FeSe_2$@SWNTs electrode was mainly due to the large particle size and insufficient interior void space of $FeSe_2$. By rational nanostructure design of active materials with sufficient interior void room, it holds great promise to boost the performance of SWNT-coated composites. As disclosed in Figure S15–16, $FeSe_2$@SWNTs exhibited higher capacitance ratio and better ion diffusion coefficient than $FeSe_2$@rGO composite for both SIBs and PIBs, further demonstrating the effect of SWNTs layer for superior rate capability.

n CONCLUSION

In summary, monodispersed SWNTs assembled coating layer has been developed to enhance the battery performance of conversion-type anode materials. The mesoporous SWNTs layer can not only enable fast electron/ion transport kinetics for superior rate behavior, but also prevent the active material from aggregation with good structure stability, thus leading to excellent Li/Na/K-ion storage performance. For lithium storage, Fe_3O_4@SWNTs composite manifested high capacity, good rate capability and long-term cycling life, outperforming other SWNT-based composites and Fe_3O_4@rGO electrode. Besides, SWNTs coating also improved the sodium/potassium storage behavior of $FeSe_2$ and realized high-rate capacities of 295 $mA{\cdot}h{\cdot}g^{-1}$ at 20 $A{\cdot}g^{-1}$ for SIBs and 171 $mA{\cdot}h{\cdot}g^{-1}$ at 10 $A{\cdot}g^{-1}$ for PIBs. This work offers a mesoporous SWNTs layer to replace graphene, which can be extended to decorate other anode materials for achieving superior high-performance metal-ion batteries.

n EXPERIMENTAL

Synthesis of Fe_3O_4@SWNTs. Hollow Fe_3O_4 was prepared via a reported solvothermal method. Typically, 5 mmol $FeCl_3{\cdot}6H_2O$, 45 mmol urea, and 1.00 g PEG-2000 were dissolved in 35 mL ethylene glycol under sonication. The above solution was transferred into a 100 mL Teflon-lined autoclave and kept at 200 °C for 48 h. Subsequently, 150 mg hollow Fe_3O_4 was stirred in 150 mL H_2O containing 1.5 mL polydiallyldimethylammonium chloride (PDDA) for 12 h, followed by washing with 1 L de-ionized water and drying at 80 °C for 12 h. Monodispersed SWNTs with abundant carboxyl and hydroxyl groups, denoted as O-SWNTs, were obtained by chemical treating commercial SWNT bundles with Hummer's method.

For SWNT coating, 25 mg PDDA-decorated Fe_3O_4 particles was sonicated in 80 mL H_2O to form a uniform solution, and then dropped into 160 mL O-SWNT solution (0.05 mg/mL) drop-by-drop and stirred for another 1 h. After vacuum-filtration and freeze drying, as-obtained sample was further heated at 300 °C for 1 h in Ar atmosphere to achieve Fe_3O_4@SWNTs composite. The Fe_3O_4@reduced graphene oxide (rGO) sample was fabricated under the same procedure by using graphene oxide (GO) solution as precursor.

Synthesis of Fe_3O_4/SWNTs and SWNTs@Fe_3O_4. Fe_3O_4/SWNTs composite was synthesized by simply mixing Fe_3O_4 with SWNTs. In a typical experiment, 27 mg hollow Fe_3O_4 and 6 mg commercial SWNTs were dispersed in 15 mL N,N-dimethylformamide solution and sonicated for 1 h. Then, the Fe_3O_4/SWNTs composite was obtained after filtrating, washing with ethanol, and drying at 80 °C for 12 h.

SWNTs@Fe_3O_4 composite was obtained by anchoring Fe_3O_4 nanoparticles on the surface of SWNTs through a hydrothermal method. In a typical experiment, 0.25 mmol $Fe(NO_3)_3{\cdot}9H_2O$ and 0.25 mmol phenylphosphonic acid were dissolved in 20 mL de-ionized water and sonicated for 10 min, followed with the addition of 4.5 mg SWNTs and 400 mg urea. The above mixture was sonicated to form a uniform solution, and then transferred into a 50 mL Teflon-lined autoclave and heated at 180 °C for 36 h. After filtration and drying, as-obtained product was calcinated at 350 °C for 1 h in Ar/H_2 to form SWNTs@Fe_3O_4 composite.

Synthesis of $FeSe_2$@SWNTs. $FeSe_2$ was obtained through a SiO_2-protection selenylation treatment of Fe_3O_4. Typically, 120 mg hollow Fe_3O_4 was dispersed into a mixed solution of 71.4 mL ethanol, 10 mL water and 3.14 mL ammonia. After being sonicated for 1 h, a mixture of 0.895 mL tetraethyl orthosilicate and 10 mL ethanol was added, followed with continuous stirring for 6 h. The Fe_3O_4@SiO_2 product and selenium power with a weight ratio of 1:15 were loaded onto an alumina crucible, and then calcinated under Ar/H_2 atmosphere at 350 °C for 10 h at a heating rate of 5 °C/min. As-produced $FeSe_2$@SiO_2 was then etched with HF solution to gain $FeSe_2$ particles. The $FeSe_2$@SWNTs composite was prepared under the same procedure with Fe_3O_4@SWNTs through PDDA modification of $FeSe_2$ followed with SWNTs coating. The $FeSe_2$@rGO was obtained under the same method with GO as the precursor.

DOI: 10.14102/j.cnki.0254-5861.2021-0050

Materials Characterization. The morphology and structure properties of the composites were investigated by transmission electron microscope (TEM, Tecani G2 F20), scanning electron microscopy (SEM, Su-8010), X-ray diffraction (XRD, Miniflex600), Raman spectroscopy (LabRam HR Evo), surface area analysis (Quantachrome Autosorb-iQ2-XR), and X-ray photoelectron spectroscopy (XPS, ESCALAB 250Xi). The weight contents of SWNTs and rGO were conducted by thermogravimetric analyses (TGA, NETZSCH STA449F3) from 30 to 800 °C at a heating rate of 10 °C in Air.

Electrochemical Measurements. The electrochemical performance of as-prepared composite was conducted via CR2025-type coin cells. The working electrodes were fabricated by blending active materials, carboxymethyl cellulose binder, and Ketjen black carbon (weight ratio of 7:1.5:1.5) with water, posting on Ni foam, and drying at 80 °C for 12 h under vacuum. The mas loading per electrode was around 0.7–1.0 mg/cm^2. For lithium storage test, lithium metal and microporous polypropylene film (Celgard 2500) were used as the counter electrode and separator, respectively. The electrolyte was 1 M $LiPF_6$ in the mixture of ethylene carbonate and dimethyl carbonate and ethylmethyl carbonate with a volume ratio of 1:1:1. For sodium storage, the counter electrode, separator, and electrolyte were sodium foil, glass fiber, and 1 M $NaClO_4$ in the mixture of ethylene carbonate and diethyl carbonate (1:1 in volume) with 5% of fluoroethylene carbonate. For potassium storage, the separator, counter electrode, and electrolyte were glass fiber, potassium foil, and 0.5 M KPF_6 in propylene carbonate and ethylene carbonate (1:1 in volume). The discharge/charge cycles were carried out under various current densities over potential ranges of 0.05–2.8 V versus Na/Na^+ or K/K^+ and 0.05–3.0 V versus Li/Li^+ through a battery testing system (LAND CT2001A). The electrochemical workstation (CHI660D) was utilized to conduct cyclic voltammetry (CV) test under various scan rates.

n ACKNOWLEDGEMENTS

This work was supported by the Science and Technology Planning Project of Fujian Province (2021J01151), CAS Key Laboratory of Design and Assembly of Functional Nanostructures (2013DP173231), the Award Program for Fujian Minjiang Scholar Professorship (2021), and the Start-up Funding from FJNU.

n AUTHOR INFORMATION

Corresponding author. Email: ifeyzhao@fjnu.edu.cn

n COMPETING INTERESTS

The authors declare no competing interests.

n ADDITIONAL INFORMATION

Supplementary information is available for this paper at http://manu30.magtech.com.cn/jghx/EN/10.14102/j.cnki.0254-5861.2021-0050

For submission: https://mc03.manuscriptcentral.com/cjsc

n REFERENCES

(1) Jung, S. K.; Hwang, I.; Chang, D.; Park, K. Y.; Kim, S. J.; Seong, W. M.; Eum, D.; Park, J.; Kim, B.; Kim, J.; Heo, J. H.; Kang, K. Nanoscale phenomena in lithium-ion batteries. *Chem. Rev.* **2020**, 120, 6684–6737.

(2) Chayambuka, K.; Mulder, G.; Danilov, D. L.; Notten, P. H. L. From Li-ion batteries toward Na-ion chemistries: challenges and opportunities. *Adv. Energy Mater.* **2020**, 10, 2001310.

(3) Hosaka, T.; Kubota, K.; Hameed, A. S.; Komaba, S. Research development on K-ion batteries. *Chem. Rev.* **2020**, 120, 6358–6466.

(4) Zhang, W.; Lu, J.; Guo, Z. Challenges and future perspectives on sodium and potassium ion batteries for grid-scale energy storage. *Mater. Today* **2021**, DOI: 10.1016/j.mattod.2021.03.015.

(5) Reddy, M. V.; Rao, G. V. S.; Chowdari, B. V. R. Metal oxides and oxysalts as anode materials for Li ion batteries. *Chem. Rev.* **2013**, 113, 5364–5457.

(6) Pan, Q. G.; Tong, Z. P.; Su, Y. Q.; Qin, S.; Tang, Y. B. Energy storage mechanism, challenge and design strategies of metal sulfides for rechargeable sodium/potassium-ion batteries. *Adv. Funct. Mater.* **2021**, 31, 2103912.

(7) Wu, Y. H.; Zhang, C. L.; Zhao, H. P.; Lei, Y. Recent advances in ferromagnetic metal sulfides and selenides as anodes for sodium- and potassium-ion batteries. *J. Mater. Chem. A* **2021**, 9, 9506–9534.

(8) Chen, M.; Zhao, J. M.; Sun, C. A. F. High-volumetric-capacity WSe_2 anode for potassium-ion batteries. *Chin. J. Struct. Chem.* **2021**, 40, 926–932.

(9) Zhao, Y.; Wang, L. P.; Sougrati, M. T.; Feng, Z. X.; Leconte, Y.; Fisher, A.; Srinivasan, M.; Xu, Z. C. A review on design strategies for carbon based metal oxides and sulfides nanocomposites for high performance Li and Na ion battery anodes. *Adv. Energy Mater.* **2017**, 7, 1601424.

(10) Wang, Y.; Fu, X. W.; Zheng, M.; Zhong, W. H.; Cao, G. Z. Strategies for building robust traffic networks in advanced energy storage devices: a focus on composite electrodes. *Adv. Mater.* **2019**, 31, 1804204.

(11) Liu, T.; Zhang, L. Y.; Cheng, B.; Yu, J. G. Hollow carbon spheres and their hybrid nanomaterials in electrochemical energy storage. *Adv. Energy Mater.* **2019**, 9, 1803900.

(12) Li, S. Y.; He, W.; Liu, B.; Cui, J. Q.; Wang, X. H.; Peng, D. L.; Liu, B.; Qu, B. H. One-step construction of three-dimensional nickel sulfide-embedded carbon matrix for sodium-ion batteries and hybrid capacitors. *Energy Storage Mater.* **2020**, 25, 636–643.

(13) Zhu, L.; Yang, X. X.; Xiang, Y. H.; Kong, P.; Wu, X. W. Neurons-system-like structured SnS_2/CNTs composite for high-performance sodium-ion battery anode. *Rare Metals* **2021**, 40, 1383–1390.

(14) Liu, B.; Lei, D. N.; Wang, J.; Zhang, Q. F.; Zhang, Y. G.; He, W.; Zheng, H. F.; Sa, B. S.; Xie, Q. S.; Peng, D. L.; Qu, B. H. 3D uniform nitrogen-doped carbon skeleton for ultra-stable sodium metal anode. *Nano Res.* **2020**, 13, 2136–2142.

(15) Xie, F. X.; Zhang, L.; Ye, C.; Jaroniec, M.; Qiao, S. Z. The application of hollow structured anodes for sodium-ion batteries: from simple to complex systems. *Adv. Mater.* **2019**, 31, 1800492.

(16) Fang, Y. J.; Luan, D. Y.; Gao, S. Y.; Lou, X. W. Rational design and engineering of one-dimensional hollow nanostructures for efficient electrochemical energy storage. *Angew. Chem. Int. Ed.* **2021**, 60, 20102–20118.

(17) Yang, S. B.; Feng, X. L.; Ivanovici, S.; Mullen, K. Fabrication of graphene-encapsulated oxide nanoparticles: towards high-performance anode materials for lithium storage. *Angew. Chem. Int. Ed.* **2010**, 49, 8408–8411.

(18) Zhang, Q. M.; Shi, Z. C.; Deng, Y. F.; Zheng, J.; Liu, G. C.; Chen, G. H. Hollow Fe_3O_4/C spheres as superior lithium storage materials. *J. Power Sources* **2012**, 197, 305–309.

(19) Ma, T. T.; Liu, X. H.; Sun, L.; Xu, Y. S.; Zheng, L. L.; Zhang, J. Strongly coupled N-doped carbon/Fe_3O_4/N-doped carbon hierarchical micro/nanostructures for enhanced lithium storage performance. *J. Energy Chem.* **2019**, 34, 43–51.

(20) Ge, J. M.; Wang, B.; Wang, J.; Zhang, Q. F.; Lu, B. G. Nature of

DOI: 10.14102/j.cnki.0254-5861.2021-0050

$FeSe_2$/N-C anode for high performance potassium ion hybrid capacitor. *Adv. Energy Mater.* **2020**, 10, 1903277.

(21) Xu, K. Q.; Shen, X. P.; Song, C. S.; Chen, H. Y.; Chen, Y.; Ji, Z. Y.; Yuan, A. H.; Yang, X. L.; Kong, L. R. Construction of rGO-encapsulated Co_3O_4-$CoFe_2O_4$ composites with a double-buffer structure for high-performance lithium storage. *Small* **2021**, 17, 2101080.

(22) Shi, X. L.; Gan, Y. M.; Zhang, Q. X.; Wang, C. Y.; Zhao, Y.; Guan, L. H.; Huang, W. A partial sulfuration strategy derived multi-yolk-shell structure for ultra-stable K/Na/Li-ion storage. *Adv. Mater.* **2021**, 33, 2100837.

(23) Li, Y. J.; Zhou, J. H.; Guo, S. D. Advanced carbon materials for non-aqueous potassium ion battery anodes. *Chin. J. Struct. Chem.* **2019**, 38, 1993–1998.

(24) Ding, H. B.; Zhou, J.; Rao, A. M.; Lu, B. A. Cell-like-carbon-microspheres for robust potassium anode. *Natl. Sci. Rev.* **2021**, 8(9).

(25) Feng, Y. G.; Shu, N.; Xie, J.; Ke, F.; Zhu, Y. W.; Zhu, J. F. Carbon-coated Fe_2O_3 hollow sea urchin nanostructures as high-performance anode materials for lithium-ion battery. *Sci. China Mater.* **2021**, 64, 307–317.

(26) Li, L.; Kovalchuk, A.; Fei, H. L.; Peng, Z. W.; Li, Y. L.; Kim, N. D.; Xiang, C. S.; Yang, Y.; Ruan, G. D.; Tour, J. M. Enhanced cycling stability of lithium-ion batteries using graphene-wrapped Fe_3O_4-graphene nanoribbons as anode materials. *Adv. Energy Mater.* **2015**, 5, 1500171.

(27) Su, F. Y.; He, Y. B.; Li, B. H.; Chen, X. C.; You, C. H.; Wei, W.; Lv, W.; Yang, Q. H.; Kang, F. Y. Could graphene construct an effective conducting network in a high-power lithium ion battery? *Nano Energy* **2012**, 1, 429–439.

(28) Zhai, Y. P.; Dou, Y. Q.; Zhao, D. Y.; Fulvio, P. F.; Mayes, R. T.; Dai, S. Carbon materials for chemical capacitive energy storage. *Adv. Mater.* **2011**, 23, 4828–4850.

(29) Yu, Q. M.; Wu, C. X.; Xu, J. X.; Zhao, Y.; Zhang, J. S.; Guan, L. H. Nest-like assembly of the doped single-walled carbon nanotubes with unique mesopores as ultrastable catalysts for high power density Zn-air battery. *Carbon* **2018**, 128, 46–53.

(30) Zhao, Y.; Shi, X. L.; Ong, S. J. H.; Yao, Q. Q.; Chen, B. B.; Hou, K.; Liu, C. T.; Xu, Z. C. J.; Guan, L. H. Enhancing the charge transportation ability of yolk-shell structure for high-rate sodium and potassium storage. *ACS Nano* **2020**, 14, 4463–4474.

(31) Liang, X.; Dai, F. H. Epoxy nanocomposites with reduced graphene oxide-constructed three-dimensional networks of single wall carbon nanotube for enhanced thermal management capability with low filler loading. *ACS Appl. Mater. Inter.* **2020**, 12, 3051–3058.

(32) Yao, Q. Q.; Gan, Y. M.; Ma, Z. J.; Qian, X. Y.; Cai, S. Z.; Zhao, Y.; Guan, L. H.; Huang, W. Approaching superior potassium storage of carbonaceous anode through a combined strategy of carbon hybridization and slfur doping. *Energy Environ. Mater.* **2021**, DOI: 10.1002/eem2.12217.

(33) Wang, K.; Huang, Y.; Wang, D.; Zhao, Y.; Wang, M.; Chen, X.; Qin, X.; Li, S. Preparation and application of hollow $ZnFe_2O_4$@PANI hybrids as high performance anode materials for lithium-ion batteries. *RSC Adv.* **2015**, 5, 107247–107253.

(34) Ban, C. M.; Wu, Z. C.; Gillaspie, D. T.; Chen, L.; Yan, Y. F.; Blackburn, J. L.; Dillon, A. C. Nanostructured Fe_3O_4/SWNT electrode: binder-free and high-rate Li-ion anode. *Adv. Mater.* **2010**, 22, E145.

(35) Zhao, Y.; Li, J. X.; Wu, C. X.; Guan, L. H. A general strategy for synthesis of metal oxide nanoparticles attached on carbon nanomaterials. *Nanoscale Res. Lett.* **2011**, 6, 71–75.

(36) Shi, X. L.; Yao, Q. Q.; Wu, H. F.; Zhao, Y.; Guan, L. H. Rational design of multi-walled carbon nanotube@hollow Fe_3O_4@C coaxial nanotubes as long-cycle-life lithium ion battery anodes. *Nanotechnology* **2019**, 30, 465402.

(37) Li, X.; Sun, X. H.; Hu, X. D.; Fan, F. R.; Cai, S.; Zheng, C. M.; Stucky, G. D. Review on comprehending and enhancing the initial Coulombic efficiency of anode materials in lithium-ion/sodium-ion batteries. *Nano Energy* **2020**, 77, 105143.

(38) Kwon, Y. H.; Park, J. J.; Housel, L. M.; Minnici, K.; Zhang, G. Y.; Lee, S. R.; Lee, S. W.; Chen, Z. M.; Noda, S.; Takeuchi, E. S.; Takeuchi, K. J.; Marschilok, A. C.; Reichmanis, E. Carbon nanotube web with carboxylated polythiophene "assist" for high-performance battery electrodes. *ACS Nano* **2018**, 12, 3126–3139.

(39) Kwon, Y. H.; Minnici, K.; Park, J. J.; Lee, S. R.; Zhang, G.; Takeuchi, E. S.; Takeuchi, K. J.; Marschilok, A. C.; Reichmanis, E. SWNT anchored with carboxylated polythiophene “links” on high-capacity Li-ion battery anode materials. *J. Am. Chem. Soc.* **2018**, 140, 5666–5669.

(40) Jiang, Y. Q.; Liu, J. P. Definitions of pseudocapacitive materials: a brief review. *Energy Environ. Mater.* **2019**, 2, 30–37.

(41) Ge, P.; Hou, H. S.; Li, S. J.; Yang, L.; Ji, X. B. Tailoring rod-like $FeSe_2$ coated with nitrogen-doped carbon for high-performance sodium storage. *Adv. Funct. Mater.* **2018**, 28, 1801765.

(42) Xu, J. L.; Zhang, X.; Miao, Y. X.; Wen, M. X.; Yan, W. J.; Lu, P.; Wang, Z. R.; Sun, Q. In-situ plantation of Fe_3O_4@C nanoparticles on reduced graphene oxide nanosheet as high-performance anode for lithium/sodium-ion batteries. *Appl. Surf. Sci.* **2021**, 546, 149163.

(43) Gu, Z. Y.; Guo, J. Z.; Zhao, X. X.; Wang, X. T.; Xie, D.; Sun, Z. H.; Zhao, C. D.; Liang, H. J.; Li, W. H.; Wu, X. L. High-ionicity fluorophosphate lattice via aliovalent substitution as advanced cathode materials in sodium-ion batteries. *Infomat* **2021**, 3, 694–704.

(44) Wu, H.; Lu, S. Y.; Xu, S. Y.; Zhao, J.; Wang, Y. K.; Huang, C.; Abdelkader, A.; Wang, W. A.; Xi, K.; Guo, Y. Z.; Ding, S. J.; Gao, G. X.; Kumar, R. V. Blowing iron chalcogenides into two-dimensional flaky hybrids with superior cyclability and rate capability for potassium-ion batteries. *Acs Nano* **2021**, 15, 2506–2519.

(45) Tan, H. T.; Feng, Y. Z.; Rui, X. H.; Yu, Y.; Huang, S. M. Metal chalcogenides: paving the way for high-performance sodium/potassium-ion batteries. *Small Methods* **2020**, 4, 1900563.

(46) An, C. S.; Yuan, Y. F.; Zhang, B.; Tang, L. B.; Xiao, B.; He, Z. J.; Zheng, J. C.; Lu, J. Graphene wrapped $FeSe_2$ nano-microspheres with high pseudocapacitive contribution for enhanced Na-ion storage. *Adv. Energy Mater.* **2019**, 9, 1900356.

Received: December 6, 2021
Accepted: December 22, 2021
Published: January 13, 2022

DOI: 10.14102/j.cnki.0254-5861.2021-0050